

<https://doi.org/10.1038/s43246-024-00453-z>

Deeply subwavelength mid-infrared phase retardation with α -MoO₃ flakes

Check for updates

Michael T. Enders¹, Mitradeep Sarkar¹, Maxime Giteau¹, Aleksandra Deeva¹, Hanan Herzig Sheinfux¹, Mehrdad Shokooh-Saremi², Frank H. L. Koppens¹ & Georgia T. Papadakis¹ ✉

Phase retardation is a cornerstone of modern optics, yet, at mid-infrared (mid-IR) frequencies, it remains a major challenge due to the scarcity of simultaneously transparent and birefringent crystals. Most materials resonantly absorb due to lattice vibrations occurring at mid-IR frequencies, and natural birefringence is weak, calling for hundreds of microns to millimeters-thick phase retarders for sufficient polarization rotation. Here, we demonstrate mid-IR phase retardation with flakes of α -MoO₃ that are more than ten times thinner than the operational wavelength, achieving 90 degrees polarization rotation within one micrometer of material. We report conversion ratios above 50% in reflection or transmission mode, and wavelength tunability by several micrometers. Our results showcase that exfoliated flakes of low-dimensional crystals can serve as a platform for mid-IR miniaturized integrated low-loss polarization control.

From understanding the early universe¹ and mapping our galaxy² to encoding quantum information in photons³, the polarization of an electromagnetic field is an important internal property of light. Controlling light's polarization is also an indispensable part of modern life⁴, spanning applications in sensing⁵, imaging⁶, microscopy⁷, and telecommunications⁸. Phase retardation in particular, the process of introducing a phase difference between two orthogonal polarization states, is a crucial building block of modern optics. This phase difference is typically introduced by a phase retarder (or wave plate), which converts between linear and circular polarization and can achieve any elliptically polarized state in-between⁹. Despite the central role phase retardation plays in manipulating photons, for a large portion of the mid-IR spectral range, namely at wavelengths above the central wavelength of the CO₂ laser of 10.6 μ m, commercial wave plates are extremely scarce.

The mid-IR spectral range is currently experiencing rapid advancements¹⁰, and the lack of phase retardation schemes in this range greatly limits technological applications and scientific discovery. For instance, efficient mid-IR polarimetry can enable probing of hot interstellar matter in our galaxy^{11,12}. Additionally, the earth's atmosphere becomes transparent in this range, making mid-IR night vision¹³ and daytime radiative cooling¹⁴ feasible and relevant, and paving the way for mid-IR communications¹⁵, where polarization control is key. Molecular vibrations also occur in the mid-IR range. Since various biological molecules are chiral, tailoring and controlling mid-IR chirality is important in various areas such

as sensing¹⁶, detection^{17,18}, and medical microscopy¹⁹. To measure or detect mid-IR chiral photons, phase retardation is a requirement.

However, crystal lattice vibrations (phonons) in solids introduce strong resonant absorption at the mid-IR frequencies in all polar dielectrics. This greatly limits the range of available materials for polarization control elements and explains the technological gap in mid-IR phase retardation. In particular, for efficient phase retardation, transparent materials with strong intrinsic material birefringence, defined as $\Delta n = |n_o - n_e|$, where n_o and n_e are the ordinary and extraordinary refractive indices of a uniaxial material, are required. Most materials that retain some degree of birefringence at mid-IR frequencies resonantly absorb. Furthermore, birefringence is a weak effect and remains below unity ($\Delta n \ll 1$) in bulk crystals, introducing major scalability challenges in integrated mid-IR photonics.

To understand this, let us consider the principle of operation of a phase retarder composed of a lossless uniaxial crystal. Its optimal thickness is given by:

$$d_{\lambda/\rho} = \frac{\lambda}{\rho \Delta n}, \quad (1)$$

where λ is the wavelength of operation. Equation (1) gives the ideal thickness ($d_{\lambda/\rho}$) for half-wave plate ($\rho = 2$) or quarter-wave plate ($\rho = 4$) operation, rotating linear polarization and converting it to circular polarization, respectively. To compensate for weak natural birefringence, for sufficient

¹ICFO – Institut de Ciències Fòniques, The Barcelona Institute of Science and Technology, Castelldefels (Barcelona), Spain. ²Department of Electrical Engineering, Ferdowsi University of Mashhad, Mashhad, Iran. ✉e-mail: georgia.papadakis@icfo.eu

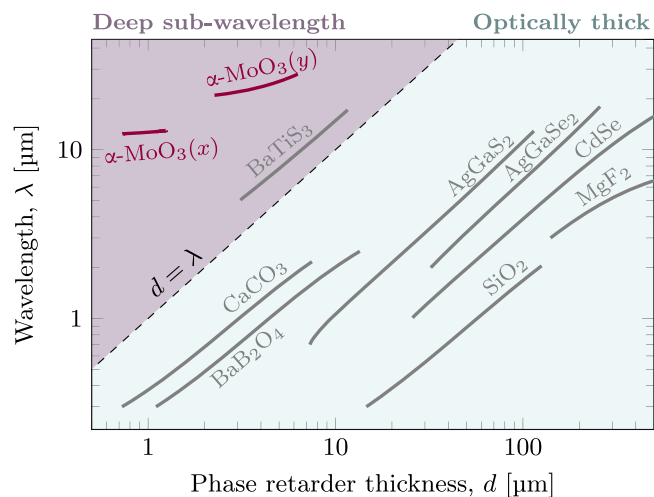


Fig. 1 | Mid-IR material comparison. Thickness and operational wavelength range for half-wave plate operation in transmission for common and state-of-the-art anisotropic materials as compared to flakes of α -MoO₃. The calculation is based on Eq. (1), and the optical constants for the considered materials are taken from⁵³: for MgF₂⁵⁴, for SiO₂⁵⁵, for CdSe⁵⁶, for AgGaSe₂⁵⁷, for AgGaS₂⁵⁸, for BaB₂O₄⁵⁴, for CaCO₃⁴⁰, for BaTiS₃.

phase retardation, wave plates have thicknesses ranging from hundreds of microns to millimeters²⁰. This is shown in the cyan highlighted region of Fig. 1, which presents a map of available birefringent materials that can operate as half-wave plates and the relevant spectral range within which they remain transparent. It can be seen that bulk materials like CaCO₃ in the near-IR or AgGaSe₂ in the mid-IR fall within the class of “optically thick” components, since they ought to be hundreds of wavelengths thick to perform as half-wave plates. The only available substitute for mid-IR wave plates are Fresnel rhomb retarders. These are delicate to align and even bulkier components, approaching in size the centimeter-scale.

To reduce size, for selected wavelengths, one can engineer form birefringence ($\Delta n > 1$), for example in liquid crystals^{21,22}, or by design, for example using dielectric, topology-optimized metasurfaces²³. In 2012, a plasmonic metasurface was introduced that operated as a quarter-wave plate in the mid-IR²⁴, with efficiency of 10%. Despite this initial demonstration, subsequent experimental investigations have been conspicuously absent, and there has been no discernible progress toward the commercialization of such structures. Form birefringence and metasurface-based induced anisotropy require various lithographic steps, and remain limited in their scalability. Reducing the dimensions of mid-IR phase retardation schemes will resolve major practical challenges including mechanical instabilities, beam incoherence, and overheating. This can enable miniaturization for on-chip and integrated optics applications, where device compactness is a requirement^{25,26}.

In this article, we leverage the properties of van der Waals (vdW), low-dimensional, in-plane anisotropic, highly dispersive materials as a platform for mid-IR phase retardation. Several low-dimensional materials, such as α -molybdenum trioxide (α -MoO₃)^{27–29} and α -vanadium oxide (α -V₂O₅)³⁰, have been recently considered for their in-plane hyperbolic dispersion, leading to a plethora of intriguing phenomena. Examples include negative refraction^{31,32} and reflection³³, reversed Cherenkov radiation³⁴, and topological^{35,36}, configurable and tunable^{32,37}, steerable³⁸ phonon polaritons. By contrast, here, we utilize the hyperbolic response of α -MoO₃ as an extreme case of birefringence to demonstrate a practical mechanism: phase retardation, for which a hyperbolic response is not a requirement. Like bulk crystals, α -MoO₃ also resonantly absorbs, nonetheless its very strong birefringence dominates, making it an excellent material platform for phase retardation, as we show below.

We start by measuring experimentally the colossal birefringence of α -MoO₃, approaching $\Delta n = 8$ (Fig. 2) near resonance, owing to the ultra-long

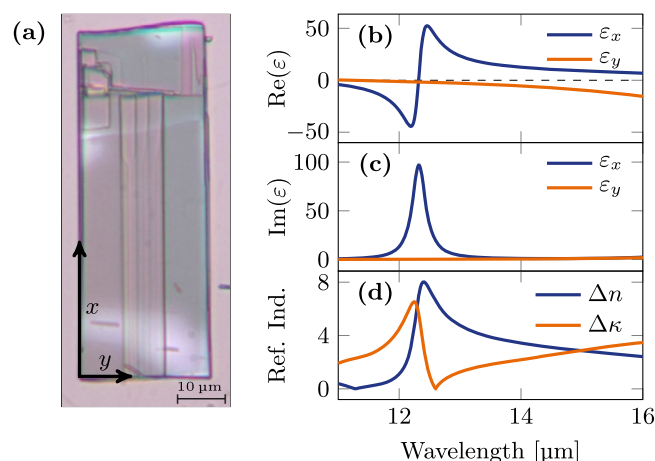


Fig. 2 | Molybdenum trioxide. **a** Microscope image of a α -MoO₃ flake where the scale bar is 10 μ m. The thickness of the flake ranges from 0.65 μ m on the right side to 0.9 μ m on the left. The x -direction represents the crystallographic direction [100] and the y -direction represents [001]. **b** Measured real and **c** imaginary part of the permittivities of the in-plane ($x - y$) directions of α -MoO₃. The method of extraction of these permittivities is described in ref. 46. **d** Birefringence $\Delta n = |n_x - n_y|$ and dichroism $\Delta \kappa = |\kappa_x - \kappa_y|$ of α -MoO₃.

lifetimes of phonon polaritons in α -MoO₃ along orthogonal crystallographic directions. This huge Δn is ideal for polarization control, as Folland and Caldwell commented in 2018³⁹. Considering the measured birefringence of α -MoO₃ and its frequency dispersion, we show in Fig. 1 that it is placed near the top-left corner of the map (purple highlighted region), in the extreme sub-wavelength regime, where the notation “ x ” and “ y ” corresponds to a phonon resonance along the x - and y -crystal direction, respectively. This map shows that by leveraging the birefringence of α -MoO₃, the required thickness for sufficient phase retardation reduces by up to three orders of magnitude with respect to the operation wavelength, as compared to conventional bulk crystals (Eq. (1)). We note that, recently, a class of quasi one-dimensional chalcogenide materials was introduced^{40,41}, having birefringence comparable to α -MoO₃ in the mid-IR. As shown in Fig. 1, BaTiS₃ could also potentially serve as a material system for mid-IR phase retardation, but no such devices have been reported.

Recently, thin-film polarizers composed of α -MoO₃ were demonstrated to reflect one linear polarization and dissipate the other⁴². Abedini Dereshgi et al. reported a mid-IR phase retarder employing α -MoO₃⁴³; however, these results pertain to heterostructure, where polarization conversion occurs due to interference effects in a thick Ge spacer interacting with α -MoO₃. The approach reported in⁴³ additionally requires multiple materials and deposition steps and transfer. These devices, only working in reflection, exhibited high resonant absorption due to the optical phonons of α -MoO₃, and could only reflect 15% of the incoming light into the cross-polarized state.

In contrast, here, we showcase that single flakes of α -MoO₃ suffice and can serve a practical material platform for miniaturized mid-IR phase retardation in either reflection or transmission, with improved performance metrics. We explain that, despite the strong frequency dispersion and resonant absorption of α -MoO₃ (Fig. 2c), insertion losses remain small due to the negligible thickness of the flakes as compared to the wavelength. We fully characterize these flakes in their operation as phase retarders, by probing experimentally the polarization rotation angle as well as the ellipticity of mid-IR photons. We note that, recently, phase retardation with α -MoO₃ was also reported at visible frequencies. In the visible range, however, the birefringence of the material is two orders of magnitude lower, and losses are negligible⁴⁴.

Our results show lithography-free phase retarders that operate at wavelengths above 10 μ m, and, to the best of our knowledge, the thinnest reported phase retarders relative to the operation wavelength. With respect

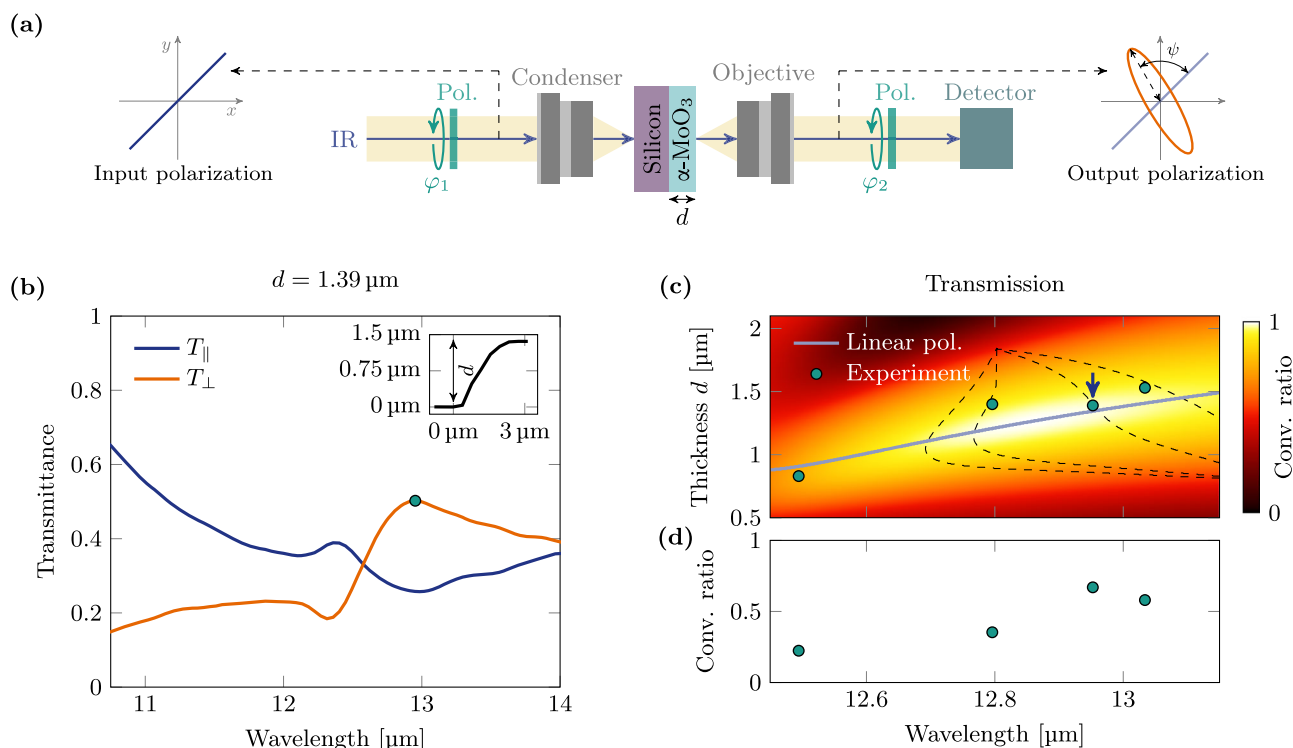


Fig. 3 | Transmittance via FTIR micro-spectroscopy. **a** Schematic of the beam path of the FTIR microscope and sample in transmission mode, including sketches of the polarization state of the incoming and outgoing light. **b** Transmittance spectra of α -MoO₃ on a Si substrate. T_{\parallel} and T_{\perp} represent the transmittance with parallel and perpendicular output polarizer, respectively, where both are normalized to the transmittance of the bare silicon substrate. Inset shows the height profile of the flake measured using AFM. **c** α -MoO₃ flake thickness d plotted against maximum

conversion wavelength. The data point obtained from the spectrum in Fig. 3b is highlighted with the arrow. The background color map shows TMM calculations of the ER, the solid light blue curve represents linear-to-linear conversion ($e = 1$), the dashed black contours mark areas where ψ is within $\pm 5^\circ$ (inner contour line) and $\pm 10^\circ$ (outer contour line) from $\psi = 90^\circ$, and the green dots are experimental data. **d** Highest conversion ratio extracted from the same flakes as in c, with thicknesses shown in the upper panel.

to existing phase retardation schemes, these retarders simultaneously reduce design complexity and material volume. The current work is a proof-of-concept demonstration of phase retardation with van der Waals anisotropic flakes and can be extended to other crystals such as α -V₂O₅ (see previous numerical results in⁴⁵), which has the same type of anisotropy as α -MoO₃ at longer wavelengths³⁰.

Results

Fabrication and characterization of α -MoO₃ flakes

We mechanically exfoliate flakes of α -MoO₃ from bulk crystals and transfer them to silicon and gold-coated glass substrates to realize phase retarders that operate in transmission and reflection mode, respectively. Exfoliated flakes of α -MoO₃ typically possess a rectangular shape, due to the crystal's orthorhombic structure²⁹ (Fig. 2a). We refer to the crystal directions [100], [001], and [010] as the x -, y -, and z -axis. We measure the dielectric permittivity of α -MoO₃ using Fourier transform infrared (FTIR) spectroscopy, implementing the method described in⁴⁶. The results we obtain, shown in Fig. 2b, c, are in agreement with previous reports^{27–29}. As shown in panel b, near $12 \mu\text{m}$, the dielectric function along the x -axis (ϵ_x) resonates due to a transverse optical phonon occurring at the corresponding photon energy, while ϵ_y remains very small. Thus, the birefringence of α -MoO₃ in this spectral region reaches values near 8.

To characterize the performance of these flakes for phase retardation, we first measure the transmittance and reflectance spectra using FTIR micro-spectroscopy. We control the input beam's polarization and read the output beam's polarization using two wire-grid polarizers, in both transmission and reflection modes, as shown in Figs. 3a and 4a, respectively. The input polarizer is oriented at 45° with respect to the crystal's axes, as shown with the blue straight line in the sketches next to the setup in Figs. 3a and 4a. They depict the polarization ellipse of the input beam with respect to the two

crystallographic axes. As a result of the input polarizer, the input polarization ellipse reduces to a straight line, oriented at an angle of 45° with respect to the x -axis. Correspondingly, the orange shape in the sketch next to the output polarizer in Figs. 3a and 4a, represents a general elliptical polarization state with arbitrary ellipticity, defined by the quantity $e = \sqrt{1 - b^2/a^2}$, with a and b being the half-lengths of the major and minor axes of the ellipse, respectively. For linearly polarized output light, the ellipse collapses into a line $e = 1$, whereas circularly polarized light traces a circle $e = 0$, corresponding to circular polarization. In the same schematics of Figs. 3a and 4a, we denote ψ , which is the rotation angle of the principal axis of the output beam's polarization ellipse, with respect to the input polarization, termed henceforth polarization rotation. In the case of a lossless dielectric crystal, the representation of a phase retarder via the pair (e , ψ) reduces to the standard description via the retardance δ ($\delta = \pi$ and $\delta = \pi/2$ correspond to a half-wave plate and quarter-wave plate operation, respectively), quoted in commercial wave plates.

Transmittance measurements

In transmission mode (Fig. 3), we define the polarization conversion ratio as $T_{\perp}/(T_{\parallel} + T_{\perp})$ and the phase retarder's insertion loss (IL) as $-10 \log(T_{\perp} + T_{\parallel})$, where T_{\perp} and T_{\parallel} are the measured transmittance with the output polarizer perpendicular and parallel to the input one, respectively. Both T_{\perp} and T_{\parallel} are normalized to $T_{\parallel,sub}$, taken on the bare silicon substrate. In this notation, therefore, T_{\perp} denotes the absolute conversion. Figure 3b shows the transmittance spectra measured for a flake of thickness $1.39 \mu\text{m}$ (inset shows the atomic force microscopy (AFM) data). As can be seen from T_{\perp} , maximum polarization rotation occurs at $12.95 \mu\text{m}$, and the absolute conversion is approximately 50%. In reflection mode (Fig. 4), R_{\parallel} and R_{\perp} correspond to the output polarizer parallel and perpendicular to the input polarizer, respectively, as shown in Fig. 4a, normalized to the gold-

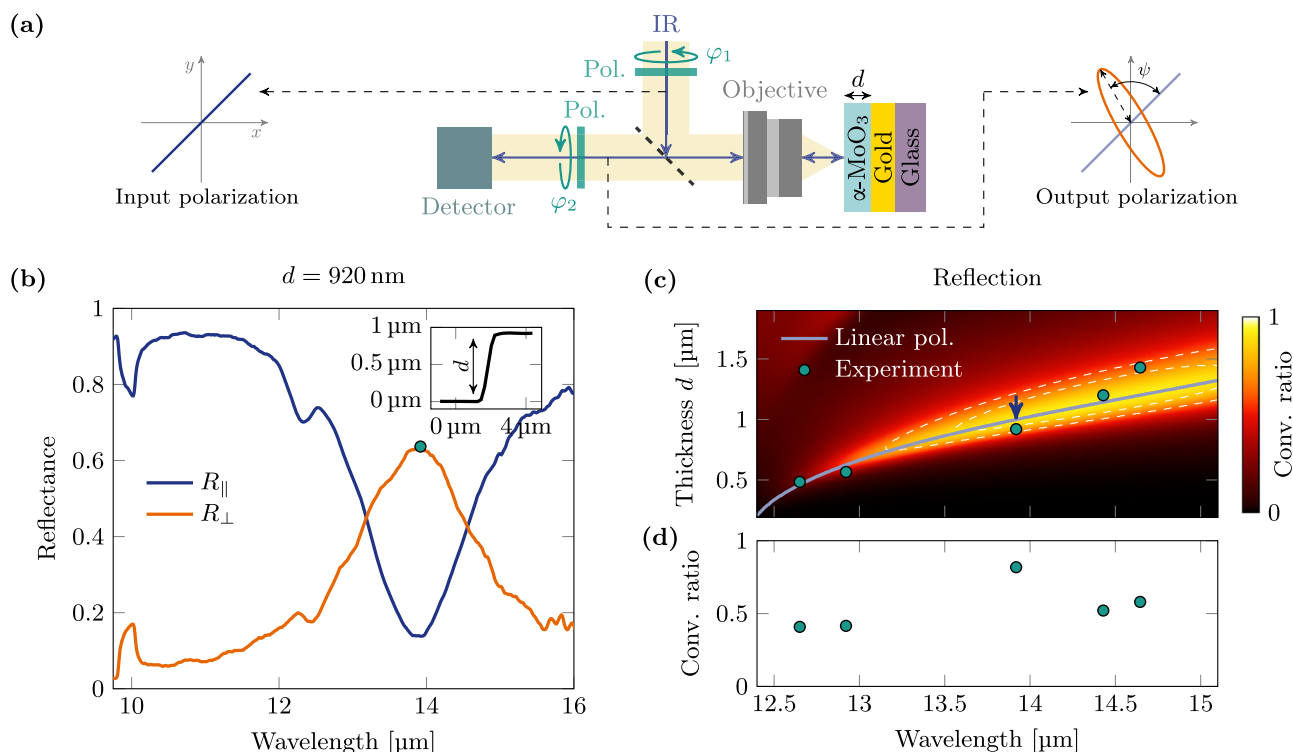


Fig. 4 | Reflectance via FTIR micro-spectroscopy. **a** Schematic showing the beam path of the FTIR microscope and the sample in reflection mode and sketches of the polarization state of the incoming and outgoing light. **b–d** show the reflectance

analogues of the corresponding panels in Fig. 3, except that the dashed black contours in **c** mark areas where the inner line shows the region where ψ exceeds 70° and the outer one where $\psi > 60^\circ$ with $\psi_{\max} = 75^\circ$.

coated substrate. We present in Fig. 4b the measured reflectance spectra for a flake of thickness 920 nm (AFM measurement in inset). For this flake, the maximum absolute conversion (R_{\perp}) is 64% near $13.9 \mu\text{m}$. The maximum conversion is determined for each flake in the same manner as in transmission mode (Fig. 3), and varies for different flakes and different wavelengths depending on thickness.

The selection of the correct thickness for phase retardation is important. Equation (1) holds within the ray optics approximation, describing appropriately optically thick and lossless dielectric wave plates. The validity of this approximation no longer holds in the presence of strong frequency dispersion (high Δn), losses, and dichroism. This is the case for the class of vdW materials considered here, where merely accounting for the phase acquired upon propagation within the slab is not sufficient and one needs to solve the full boundary problem to appropriately determine the correct thickness for half-wave plate operation⁴⁷. In Supplementary Fig. S10, we demonstrate that, within the spectral region of the Reststrahl band of $\alpha\text{-MoO}_3$ and for flake thicknesses in the range of one micrometer, the condition $\delta = \pi$ is satisfied. This range of thicknesses is extremely small as compared to the wavelength, a result of the ultra-high birefringence of $\alpha\text{-MoO}_3$ on-resonance. As shown there, the strong frequency dispersion and large Δn of $\alpha\text{-MoO}_3$ in that spectral region yields strong sensitivity of the optimal operational wavelength with respect to small changes in a flake's thickness.

We use an in-house implementation of the transfer matrix method (TMM)^{48,49} to show in Figs. 3c and 4c color maps of the calculated polarization conversion ratio in transmission and reflection mode, respectively, as a function of flake's thickness and wavelength for which polarization rotation ψ approaches 90 degrees (see Supplementary Figs. S11 and S12). This occurs in the vicinity of thicknesses near $1 \mu\text{m}$ and for wavelengths near $12.5 \mu\text{m}$, where birefringence is maximal. This is predicted for the condition $\delta = \pi$ (Supplementary Fig. S10).

The solid light blue curve in Fig. 3c shows the points where the output polarization is expected to be purely linear. The maximum conversion ratio is achieved when $\psi = 90^\circ$ along this line. The dashed black contours mark the

areas where ψ is within $\pm 5^\circ$ (inner contour line) and $\pm 10^\circ$ (outer contour line) from $\psi = 90^\circ$. Experimental results are superimposed and shown as green dots, each corresponding to a particular flake with given thickness (x -axis). The wavelength at which each measured data point is placed corresponds to the wavelength at which optimal polarization conversion (y -axis) was measured. The full spectra for all measured flakes are shown in Supplementary Fig. S3. We observe good agreement between the experimental results and the numerical results for half-wave plate operation. Notably, three of our measurements, corresponding to three different flakes with different thicknesses, fall within a polarization rotation angle range between 80° to 100° with high conversion ratios. From Fig. 3d, the maximum experimentally measured polarization conversion ratio is 0.67, and is achieved for $d \approx 1.4 \mu\text{m}$ for the wavelength of $12.95 \mu\text{m}$ as shown by the vertical arrow. For all the experimental data points, the IL remains below 1.3 dB. By adding reflections from the Si substrate, the net IL is 4.1 dB. The losses due to the Si substrate are easily mitigated with an anti-reflection coating. The low insertion loss despite the absorption of $\alpha\text{-MoO}_3$ is expected, owing to the deeply subwavelength thickness of the flakes.

Reflectance measurements

Similarly, in reflection mode, the green data points in Fig. 4c represent these experimental results, and are superimposed with the corresponding TMM numerical calculations. The solid light blue curve corresponds to pure linear polarization with $e = 1$. Unlike the transmission mode, in reflection mode, due to additional losses in the Au, the maximum predicted polarization rotation ψ deviates from 90° , as also verified experimentally (Fig. 5). The maximum polarization rotation angle predicted is 75° . The regions where ψ exceeds 70° and 60° are depicted by the inner and outer black dashed contour lines in white, respectively. The area enclosed by these inner contours represents operation as close as possible to half-wave plate in reflection mode. Experimentally, although we do not expect maximal polarization rotation of 90° , we still measure considerably high conversion ratio from one polarization state to its orthogonal counterpart. In reflection mode, light

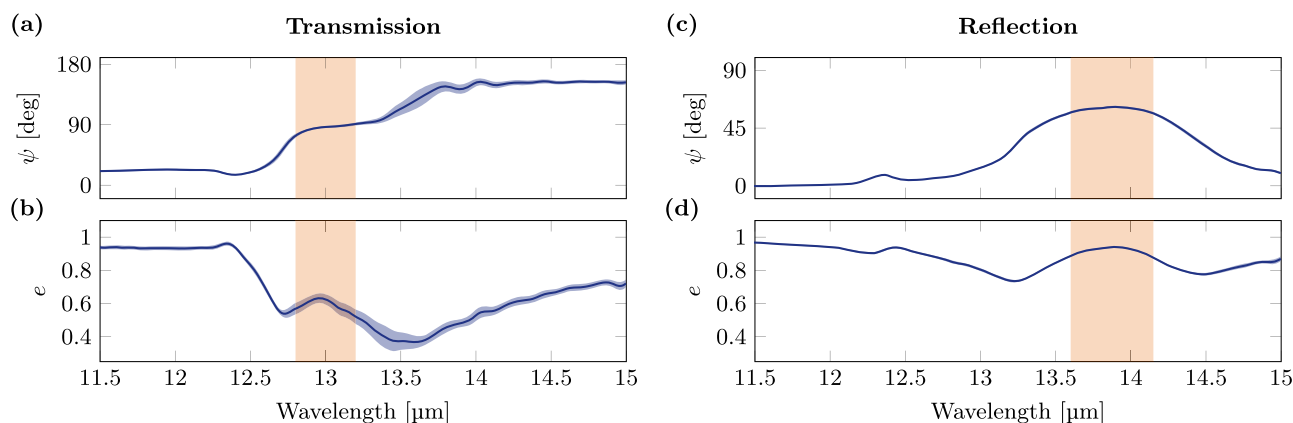


Fig. 5 | Polarization state characterization. The polarization rotation angle ψ of the transmitted and reflected beam in each mode of operation are reconstructed in a transmission (flake thickness: 1.39 μm , silicon substrate) and c reflection (flake thickness: 0.92 μm , on Au). The ellipticity e for transmission and reflection is shown

in **b** and **d**, respectively. The ribbon around the lines shows the standard deviation of the numerically fitted parameters (see Supplementary Figs. S8 and S9). The orange-shaded region shows the spectral range where the rotation ψ is close to 90°.

traverses the flake twice, thus experiencing the strong birefringence twice. This yields high conversion for a wider range of wavelengths than in transmission mode, as expected. This is shown in Fig. 4c, where one can observe the potential to passively tune the operational wavelength and achieve linear polarization conversion by controlling the thickness of the flake within the range of 0.45 μm to 1.5 μm . This enables operation within the wavelength range of 12.6 μm to 15 μm , covering the entire Reststrahlen band of the $\alpha\text{-MoO}_3$ (Fig. 2b). Finally, as shown in Fig. 4d, we obtain conversion ratios up to 0.82, with IL remaining below 1.7 dB for all measured flakes.

Retrieval of the output polarization state

The results in Figs. 3 and 4 describe the intensity of the output beam's component that is 90 degrees rotated with respect to the input beam's polarization. Nonetheless, these measurements do not suffice in characterizing a phase retarder. In particular in the case of considerable frequency dispersion and absorption (Fig. 2b, c), one ought to measure the ellipticity of the output beam, as linear polarization is not necessarily preserved. To do this explicitly (while probing depolarization and handedness), the mere use of two polarizers is insufficient, as one requires an additional phase retarder. Nonetheless, as mentioned in the introduction, commercial phase retarders are not available in the mid-IR range. Hence, instead, following basic principles of ellipsometry⁵⁰, we illuminate the samples with linearly polarized light and measure the outgoing light in two configurations while rotating the sample: with the two linear polarizers parallel and orthogonal to each other (see Supplementary Figs. S4 to S7). Assuming absence of depolarization, as expected in the deep-subwavelength range that these $\alpha\text{-MoO}_3$ flakes operate, via a numerical fit to the experimental data (Supplementary Note 3), we determine ψ and e as a function of the wavelength⁵¹. These are shown in Fig. 5a and c for transmission and reflection mode, respectively, whereas the corresponding ellipticity is shown in Fig. 5b, c. The absolute retardance (δ) is shown in Supplementary Fig. S8.

As shown in Fig. 5a, in transmission mode, the polarization rotation angle reaches 90 degrees for the spectral range from 12.8 μm to 13.2 μm , as was initially designed. The ellipticity of the transmitted beam (Fig. 5b), however, deviates from the ideal value of unity. In reflection mode, as shown in Fig. 5c, the polarization rotation approaches 62 degrees, as expected from our simulations shown in Fig. 4c, while the ellipticity approaches unity, as shown in Fig. 5d, for the entire wavelength range for which the phase retarder was designed, as highlighted in the orange shaded region from 13.6 μm to 14.15 μm . This shows that linear polarization is preserved while being rotated. Deviations from the ideal half-wave plate operation arise due to losses, dichroism, and the strong sensitivity of the optimal operation wavelength with respect to the flake's thickness. These deviations are easily

corrected by properly aligning an output polarizer. Unlike phase retarders, polarizers do exist in the mid-IR range. Alternatively, as discussed below, for this new class of phase retarders, via appropriate optimization, it is always possible to approach optimal operation ($e = 1$ and $\psi = 90$ degrees) for this wavelength range with $\alpha\text{-MoO}_3$, without any additional components, through slight adjustments to the flake's thickness and experimental setup.

Discussion

We design and characterize a wide range of phase retarders composed solely of exfoliated flakes of $\alpha\text{-MoO}_3$. By controlling the flakes' thicknesses, we demonstrate polarization rotation in both transmission and reflection mode, with conversion ratios as high as 82%. Phase retardation is demonstrated over the spectral range from 12 μm to 15 μm , where bulk crystals perform poorly and commercial phase retarders are not readily available. Due to the deeply subwavelength thickness of the flakes, the absorption of $\alpha\text{-MoO}_3$ does not considerably affect the performance of the phase retarders, and insertion losses remain extremely low. Nonetheless, the losses introduce a degree of circular polarization upon transmission, which, however, can be corrected by further adjusting the flakes' thickness, or using commercial polarizers.

Our experimental results demonstrate that naturally in-plane anisotropic vdW materials can serve as highly efficient phase retarders. This phase retardation is not associated with the hyperbolic dispersion of $\alpha\text{-MoO}_3$, but is rather the result of phonon polariton resonances occurring at different frequencies along different crystal axes.

As shown in Fig. 5, the ellipticity of the phase retarded beam in transmission mode (Fig. 5b) and the polarization rotation angle in reflection mode (Fig. 5c) slightly deviate from the ideal half-wave plate operation. These can be easily corrected, for instance, by eliminating any output circularly polarized field component using another polarization element on the flake, or by directly etching a wire grid structure into the sample. Most importantly, however, in Supplementary Note 4 we carry out an rigorous analysis of phase retardation in the presence of loss and dichroism⁴⁷. From there (Supplementary Fig. S10) one can see that, for the wavelengths of interest, within the Reststrahlen band of $\alpha\text{-MoO}_3$, one can always find a combination of wavelength, thickness, and rotation angle of the input polarization with respect to the crystal axes, for which a orthogonal purely linear output polarization state ($e = 1$) is guaranteed.

Our results open new possibilities for practical applications in the mid-IR spectral range, particularly beyond the wavelengths of 10 μm , where conventional bulk materials perform poorly. The principle of operation of the phase retardation scheme discussed in this work is general and applies to any polar dielectric low-dimensional anisotropic medium. Thus, these results can be generalized to other spectral ranges, where other materials

exhibit Reststrahlen bands, for example near $18\ \mu\text{m}$ using $\alpha\text{-V}_2\text{O}_5$ ³⁰ or even to $\alpha\text{-MoO}_3$ itself for the resonance occurring along the y -direction (see Fig. 1 and Supplementary Fig. S13). As crystal growth techniques continue to improve, emerging vdW materials like $\alpha\text{-MoO}_3$ offer a new paradigm as polarization control elements, beyond the reach of conventional materials for integrated on-chip photonic devices.

Methods

Exfoliation and characterization of $\alpha\text{-MoO}_3$ flakes

The $\alpha\text{-MoO}_3$ flakes were mechanically exfoliated from bulk crystals (2D Semiconductors) by means of polydimethylsiloxane based exfoliation (X0 retention, DGL type, Gelpak) and subsequently transferred to their respective substrate at 90° . Undoped silicon was chosen as the substrate for transmission measurements due to its high transparency and flat dispersion characteristics within the relevant wavelength range of $10\ \mu\text{m}$ to $16\ \mu\text{m}$. To conduct reflection measurements, $\alpha\text{-MoO}_3$ flakes were transferred onto a glass substrate that had been evaporation coated with a $100\ \text{nm}$ layer of gold, serving as a back reflector. The thickness profiles of individual flakes were extracted from AFM traces (Park NX20) captured with a non-contact cantilever (AC160TS, Olympus). The silicon and gold substrates were characterized using a IR-VASE Mark II ellipsometer from J.A. Woollam (see Supplementary Figs. S1 and S2).

FTIR micro-spectroscopy

We conducted FTIR micro-spectroscopy measurements using a Bruker Hyperion 2000 microscope coupled with a Bruker Tensor II FTIR spectrometer equipped with a mercury cadmium telluride detector (spectral range: $600\ \text{cm}^{-1}$ to $8000\ \text{cm}^{-1}$). A $\times 36$ Cassegrain objective was employed for collection. For transmission measurements a $\times 15$ Cassegrain objective was used as a condenser. Detailed schematics of the setup are available in ref. 52. We utilized two linear ZnSe holographic wire grid polarizers from Thorlabs to control input and output polarization. The size of the measured area was controlled using the knife-edge aperture of the microscope. The full spectra used in Figs. 3 and 4 are shown in Supplementary Note 2.

Data availability

The authors declare that all relevant data were available in this paper and its supporting information and that data supporting the results of this study are available from corresponding authors upon reasonable request.

Code availability

The code used for the TMM simulations is available at <https://doi.org/10.5281/zenodo.7974658>.

Received: 20 November 2023; Accepted: 28 January 2024;

Published online: 16 February 2024

References

- Kamionkowski, M. & Kovetz, E. D. The Quest for B modes from inflationary gravitational waves. *Ann. Rev. Astron. Astrophys.* **54**, 227–269 (2016).
- Hu, Y. & Lazarian, A. Probing 3D magnetic fields – I. Polarized dust emission. *Monthly Not. R. Astron. Soc.* **519**, 3736–3748 (2023).
- Zhang, Q. et al. Demonstration of a scheme for the generation of “event-ready” entangled photon pairs from a single-photon source. *Phys. Rev. A* **77**, 062316 (2008).
- Ding, F., Tang, S. & Bozhevolnyi, S. I. Recent advances in polarization-encoded optical metasurfaces. *Adv. Photon. Res.* **2**, 2000173 (2021).
- Lee, G. H. et al. Stretchable PPG sensor with light polarization for physical activity-permissible monitoring. *Sci. Adv.* **8**, eabm3622 (2023).
- Zhou, S. et al. Polarization-dispersive imaging spectrometer for scattering circular dichroism spectroscopy of single chiral nanostructures. *Light Sci. Appl.* **11**, 64 (2022).
- Intaravanne, Y. et al. Color-selective three-dimensional polarization structures. *Light Sci. Appl.* **11**, 302 (2022).
- Wang, H. L., Ma, H. F. & Cui, T. J. A polarization-modulated information metasurface for encryption wireless communications. *Adv. Sci.* **9**, 2204333 (2022).
- Yariv, A. & Yeh, P. *Optical waves in crystal propagation and control of laser radiation* (Wiley, 1983). <https://www.osti.gov/biblio/5951989>.
- Caldwell, J. D. & Novoselov, K. S. Mid-infrared nanophotonics. *Nat. Mater.* **14**, 364–366 (2015).
- Draine, B. T. & Hensley, B. S. The dielectric function of “Astrodrust” and predictions for polarization in the 3.4 and $10\ \mu\text{m}$ features. *Astrophys. J.* **909**, 94 (2021).
- Packham, C. et al. Design of a mid-IR polarimeter for SOFIA. In *Proc. SPIE*, vol. 7014, 70142H (2008).
- Konstantatos, G. Current status and technological prospect of photodetectors based on two-dimensional materials. *Nat. Commun.* **9**, 5266 (2018).
- Raman, A. P., Anoma, M. A., Zhu, L., Rephaeli, E. & Fan, S. Passive radiative cooling below ambient air temperature under direct sunlight. *Nature* **515**, 540–544 (2014).
- Zou, K. et al. High-capacity free-space optical communications using wavelength- and mode-division-multiplexing in the mid-infrared region. *Nat. Commun.* **13**, 7662 (2022).
- Bareza, N. J. et al. Phonon-enhanced mid-infrared CO_2 gas sensing using boron nitride nanoresonators. *ACS Photon.* **9**, 34–42 (2022).
- Huo, N., Gupta, S. & Konstantatos, G. $\text{MoS}_2\text{-HgTe}$ quantum dot hybrid photodetectors beyond $2\ \mu\text{m}$. *Adv. Mater.* **29**, 1606576 (2017).
- Wang, F. et al. A two-dimensional mid-infrared optoelectronic retina enabling simultaneous perception and encoding. *Nat. Commun.* **14**, 1938 (2023).
- Kviatkovsky, I., Chrzanowski, H. M., Avery, E. G., Bartolomaeus, H. & Ramelow, S. Microscopy with undetected photons in the mid-infrared. *Sci. Adv.* **6**, eabd0264 (2020).
- Dai, M. et al. On-chip mid-infrared photothermoelectric detectors for full-Stokes detection. *Nat. Commun.* **13**, 4560 (2022).
- Marco, D. et al. Customized depolarization spatial patterns with dynamic retardance functions. *Sci. Rep.* **11**, 9415 (2021).
- Herman, J. & Kula, P. Design of new super-high birefringent isothiocyanato bistolanes – synthesis and properties. *Liquid Cryst.* **44**, 1462–1467 (2017).
- Shi, Z. et al. Continuous angle-tunable birefringence with freeform metasurfaces for arbitrary polarization conversion. *Sci. Adv.* **6**, eaba3367 (2023).
- Yu, N. et al. A broadband, background-free quarter-wave plate based on plasmonic metasurfaces. *Nano Lett.* **12**, 6328–6333 (2012).
- Lin, Z. et al. High-performance polarization management devices based on thin-film lithium niobate. *Light Sci. Appl.* **11**, 93 (2022).
- Zhou, H. et al. All-in-one silicon photonic polarization processor. *Nanophotonics* **8**, 2257–2267 (2019).
- Ma, W. et al. In-plane anisotropic and ultra-low-loss polaritons in a natural van der Waals crystal. *Nature* **562**, 557–562 (2018).
- Zheng, Z. et al. Highly confined and tunable hyperbolic phonon polaritons in Van Der Waals semiconducting transition metal oxides. *Adv. Mater.* **30**, 1705318 (2018).
- Álvarez-Pérez, G. et al. Infrared permittivity of the biaxial van der Waals semiconductor $\alpha\text{-MoO}_3$ from near- and far-field correlative studies. *Adv. Mater.* **32**, 1908176 (2020).
- Taboada-Gutiérrez, J. et al. Broad spectral tuning of ultra-low-loss polaritons in a van der Waals crystal by intercalation. *Nat. Mater.* **19**, 964–968 (2020).
- Sternbach, A. J. et al. Negative refraction in hyperbolic hetero-bicrystals. *Science* **379**, 555–557 (2023).
- Hu, H. et al. Gate-tunable negative refraction of mid-infrared polaritons. *Science* **379**, 558–561 (2023).

33. Álvarez-Pérez, G. et al. Negative reflection of nanoscale-confined polaritons in a low-loss natural medium. *Sci. Adv.* **8**, eabp8486 (2022).
34. Guo, X. et al. Mid-infrared analogue polaritonic reversed Cherenkov radiation in natural anisotropic crystals. *Nat. Commun.* **14**, 2532 (2023).
35. Hu, G. et al. Topological polaritons and photonic magic angles in twisted α -MoO₃ bilayers. *Nature* **582**, 209–213 (2020).
36. Duan, J. et al. Enabling propagation of anisotropic polaritons along forbidden directions via a topological transition. *Sci. Adv.* **7**, eabf2690 (2021).
37. Chen, M. et al. Configurable phonon polaritons in twisted α -MoO₃. *Nat. Mater.* **19**, 1307–1311 (2020).
38. Dai, Z. et al. Edge-oriented and steerable hyperbolic polaritons in anisotropic van der Waals nanocavities. *Nat. Commun.* **11**, 6086 (2020).
39. Folland, T. G. & Caldwell, J. D. Precise control of infrared polarization. *Nature* **562**, 499–501 (2018).
40. Niu, S. et al. Giant optical anisotropy in a quasi-one-dimensional crystal. *Nat. Photon.* **12**, 392–396 (2018).
41. Mei, H. et al. Colossal optical anisotropy from atomic-scale modulations (2023).
42. Sahoo, N. R. et al. High temperature Mid-IR polarizer via natural in-plane hyperbolic Van der Waals crystals. *Adv. Opt. Mater.* **10**, 2101919 (2022).
43. Abedini Dereshgi, S. et al. Lithography-free IR polarization converters via orthogonal in-plane phonons in α -MoO₃ flakes. *Nat. Commun.* **11**, 9 (2020).
44. Abedini Dereshgi, S. et al. Low-symmetry α -MoO₃ heterostructures for wave plate applications in visible frequencies. *Adv. Opt. Mater.* **11**, 2202603 (2023).
45. Dixit, S., Sahoo, N. R., Mall, A. & Kumar, A. Mid infrared polarization engineering via sub-wavelength biaxial hyperbolic van der Waals crystals. *Sci. Rep.* **11**, 6612 (2021).
46. Sarkar, M. et al. Retrieving optical parameters of emerging van der Waals flakes (2023). 2305.13994.
47. Holmes, D. A. Exact Theory of Retardation Plates. *JOSA* **54**, 1115–1120 (1964).
48. Passler, N. C. & Paarmann, A. Generalized 4×4 matrix formalism for light propagation in anisotropic stratified media: study of surface phonon polaritons in polar dielectric heterostructures. *J. Opt. Soc. Am. B* **34**, 2128 (2017).
49. Enders, M. T. GeneralizedTransferMatrixMethod.jl.
50. Tompkins, H. & Irene, E. A. *Handbook of ellipsometry* (William Andrew, 2005).
51. Kilchoer, C., Abdollahi, N., Steiner, U., Gunkel, I. & Wilts, B. D. Determining the complex Jones matrix elements of a chiral 3D optical metamaterial. *APL Photonics* **4**, 126107 (2019).
52. Folland, T. G., Nordin, L., Wasserman, D. & Caldwell, J. D. Probing polaritons in the mid- to far-infrared. *J. Appl. Phys.* **125**, 191102 (2019).
53. Dodge, M. J. Refractive properties of magnesium fluoride. *Appl. Opt.* **23**, 1980–1985 (1984).
54. Ghosh, G. Dispersion-equation coefficients for the refractive index and birefringence of calcite and quartz crystals. *Optics Communications* **163**, 95–102 (1999).
55. Lisitsa, M. P., Gudymenko, L. F., Malinko, V. N. & Terekhova, S. F. Dispersion of the refractive indices and birefringence of CdSxSe1-x single crystals. *Physica Status Solidi (b)* **31**, 389–399 (1969).
56. Kato, K., Miyata, K. & Petrov, V. Refined Sellmeier equations for AgGaSe₂ up to 18 μm . *Appl. Opt.* **60**, 805–808 (2021).
57. Kato, K. K. & Shirahata, H. S. H. Nonlinear IR Generation in AgGaS₂. *Jpn J. Appl. Phys.* **35**, 4645 (1996).
58. Tamošauskas, G., Beresnevičius, G., Gadonas, D. & Dubietis, A. Transmittance and phase matching of BBO crystal in the 3–5 μm

range and its application for the characterization of mid-infrared laser pulses. *Opt. Mater. Exp.* **8**, 1410–1418 (2018).

Acknowledgements

We thank V. Pruneri for generously granting access to his laboratory and equipment, as well as engaging in fruitful discussions. G.T.P. acknowledges financial support from the la Caixa Foundation (ID 100010434). M.E. acknowledges financial support from MCIN/AEI/10.13039/501100011033 (PRE2020-094401) and FSE “El FSE invierte en tu futuro”. M. G. acknowledges financial support from the Severo Ochoa Excellence Fellowship. This work was supported by the Spanish MICINN (PID2021-125441OA-I00, PID2020-112625GB-I00, and CEX2019-000910-S), the European Union (fellowship LCF/BQ/PI21/11830019 under the Marie Skłodowska-Curie Grant Agreement No. 847648), Generalitat de Catalunya (2021 SGR 01443) through the CERCA program, Fundació Cellex, and Fundació Mir-Puig. F.H.L.K. acknowledges support from the ERC TOPO-NANOP (726001), the government of Spain (PID2019-106875GB-I00) and Generalitat de Catalunya (CERCA, AGAUR, 2021 SGR 01443). Furthermore, the research leading to these results has received funding from the European Union’s Horizon 2020 under grant agreement no. 881603 (Graphene flagship Core3) and 820378 (Quantum flagship).

Author contributions

Conceptualization GTP Formal Analysis MTE, MS, MG Funding acquisition FHLK, GTP Investigation MTE, MS Methodology MTE, MS Resources HHS, FHLK, GTP Software MTE Visualization MTE Writing—original draft MTE Writing—review & editing MTE, MS, AD, MG, HHS, MSS, FK, GTP.

Competing interests

The authors declare no competing interests.

Additional information

Supplementary information The online version contains supplementary material available at <https://doi.org/10.1038/s43246-024-00453-z>.

Correspondence and requests for materials should be addressed to Georgia T. Papadakis.

Peer review information *Communications Materials* thanks the anonymous reviewers for their contribution to the peer review of this work. Primary Handling Editors: Aldo Isidori. A peer review file is available.

Reprints and permissions information is available at <http://www.nature.com/reprints>

Publisher’s note Springer Nature remains neutral with regard to jurisdictional claims in published maps and institutional affiliations.

Open Access This article is licensed under a Creative Commons Attribution 4.0 International License, which permits use, sharing, adaptation, distribution and reproduction in any medium or format, as long as you give appropriate credit to the original author(s) and the source, provide a link to the Creative Commons licence, and indicate if changes were made. The images or other third party material in this article are included in the article’s Creative Commons licence, unless indicated otherwise in a credit line to the material. If material is not included in the article’s Creative Commons licence and your intended use is not permitted by statutory regulation or exceeds the permitted use, you will need to obtain permission directly from the copyright holder. To view a copy of this licence, visit <http://creativecommons.org/licenses/by/4.0/>.

© The Author(s) 2024